

EPIC 211391664 B: A 32- M_{\oplus} NEPTUNE-SIZED PLANET IN A 10-DAY ORBIT TRANSITING AN F8 STAR

OSCAR BARRAGÁN¹, SASCHA GRZIWA², DAVIDE GANDOLFI^{1,3}, MALCOLM FRIDLUND^{4,5}, MICHAEL ENDL⁶, HANS J. DEEG^{7,8},
MANUEL P. CAGIGAL⁹, ANTONINO F. LANZA¹⁰, PIER G. PRADA MORONI^{11,12}, ALEXIS SMITH¹³, JUDITH KORTH²,
MEGAN BEDELL¹⁴, JUAN CABRERA¹³, WILLIAM D. COCHRAN⁶, FELICE CUSANO¹⁵, SZILARD CSIZMADIA¹³,
PHILIPP EIGMÜLLER¹³, ANDERS ERIKSON¹³, EIKE W. GUENTHER¹⁶, ARTIE P. HATZES¹⁶, DAVID NESPRAL^{7,8},
MARTIN PÄTZOLD², JORGE PRIETO-ARRANZ^{7,8}, AND HEIKE RAUER^{13,17}

¹Dipartimento di Fisica, Università di Torino, via P. Giuria 1, 10125 Torino, Italy; oscar.barraganvil@edu.unito.it

²Rheinisches Institut für Umweltforschung an der Universität zu Köln, Aachener Strasse 209, 50931 Köln, Germany

³Landessternwarte Königstuhl, Zentrum für Astronomie der Universität Heidelberg, Königstuhl 12, 69117 Heidelberg, Germany

⁴Leiden Observatory, University of Leiden, PO Box 9513, 2300 RA, Leiden, The Netherlands

⁵Department of Earth and Space Sciences, Chalmers University of Technology, Onsala Space Observatory, 439 92 Onsala, Sweden

⁶Department of Astronomy and McDonald Observatory, University of Texas at Austin, 2515 Speedway, Stop C1400, Austin, TX 78712, USA

⁷Instituto de Astrofísica de Canarias, 38205 La Laguna, Tenerife, Spain

⁸Departamento de Astrofísica, Universidad de La Laguna, 38206 La Laguna, Spain

⁹Departamento de Física Aplicada, Universidad de Cantabria Avenida de los Castros s/n, E-39005 Santander, Spain

¹⁰INAF - Osservatorio Astrofisico di Catania, via S. Sofia 78, 95123, Catania, Italy

¹¹Physics Department "E. Fermi", University of Pisa, Largo B. Pontecorvo 3, 56127, Pisa, Italy

¹²Istituto Nazionale di Fisica Nucleare, Largo B. Pontecorvo 3, 56127, Pisa, Italy

¹³Institute of Planetary Research, German Aerospace Center, Rutherfordstrasse 2, 12489 Berlin, Germany

¹⁴Department of Astronomy and Astrophysics, University of Chicago, 5640 S. Ellis Ave, Chicago, IL 60637, USA

¹⁵INAF Osservatorio Astronomico di Bologna, Via Ranzani, 1, 40127, Bologna

¹⁶Thüringer Landessternwarte Tautenburg, Sternwarte 5, D-07778 Tautenburg, Germany

¹⁷Center for Astronomy and Astrophysics, TU Berlin, Hardenbergstr. 36, 10623 Berlin, Germany

ABSTRACT

We report the discovery of EPIC 211391664b, a transiting Neptune-sized planet monitored by the K2 mission during its campaign 5. We combine the K2 time-series data with ground-based photometric and spectroscopic follow-up observations to confirm the planetary nature of the object and derive its mass, radius, and orbital parameters. EPIC 211391664b is a warm Neptune-like planet in a 10-day orbit around a $V=12.2$ mag F-type star with $M_{\star}=1.074 \pm 0.042 M_{\odot}$, $R_{\star}=1.311^{+0.083}_{-0.048} R_{\odot}$, and age of $5.2^{+1.2}_{-1.0}$ Gyr. We derive a planetary mass and radius of $M_p = 32.2 \pm 8.1 M_{\oplus}$ and $R_p = 4.3^{+0.3}_{-0.2} R_{\oplus}$. EPIC 211391664 b joins the relatively small group of Neptune-sized planets whose mass and radius have been derived with a precision better than $3\text{-}\sigma$. We estimate that the planet will be engulfed by EPIC 211391664 in ~ 3 Gyr, due to the evolution of the host star towards the red giant branch.

Keywords: planets and satellites: detection — planets and satellites: individual: EPIC 211391664b — stars: fundamental parameters

1. INTRODUCTION

The transit of an exoplanet in front of its host star provides us with valuable information about its size. When combined with radial velocity (RV) measurements (e.g., [Mayor & Queloz 1995](#)) or transit timing variations (TTVs, e.g., [Ford et al. 2011](#)), transit photometry gives us access to the geometry of the orbit, enabling the measurement of the true mass of the planet, of its radius, and consequently of its mean density. Masses, radii, densities, and orbital parameters are fundamental “in-

gredients” to study the internal structure, composition, dynamical evolution, tidal interaction, architecture, and atmosphere of exoplanets (e.g., [Winn & Fabrycky 2015](#); [Hatzes 2016](#)).

The space-based photometry revolution of *CoRoT* ([Baglin et al. 2006](#)) and *Kepler* ([Borucki et al. 2010](#)) has given us access to the small-radius planet domain ($R_p \lesssim 6 R_{\oplus}$, i.e., Neptune- and Earth-sized planets), a regime that is not easily accessible from the ground. Neptune-like planets ($2.0 \lesssim R_p \lesssim 6.0 R_{\oplus}$,

$10 \lesssim M_p \lesssim 40 M_\oplus$ (Borucki et al. 2011) are of special interest as they mark the transition from Super-Earths to larger planets with higher volatile content, more akin to the icy giants in our solar system. However, our knowledge of these planets is still quite limited. Although *Kepler* has found that $\sim 26\%$ of Sun-like stars in our Galaxy host small planets with orbital period shorter than 100 days (Marcy et al. 2014), determinations of masses at a $3\text{-}\sigma$ level – or better – have been possible only for a few dozen Neptune-like planets¹. This is because of the small RV variations induced by such planets and the faintness of most of the *Kepler* host stars ($V > 13$ mag), which makes them not suitable for precise RV follow-up observations.

The K2 mission – after the nominal *Kepler* mission lost two reaction wheels – is an unique opportunity to gain knowledge of Neptune-sized planets. K2 is targeting stars 15 times brighter than those targeted by the original *Kepler* mission (Howell et al. 2014), a definitive advantage for any RV follow-up.

As part of the KEST, ESPRINT, and PICK2 collaborations (Cochran et al. 2015; Grziwa et al. 2015; Sanchis-Ojeda et al. 2015; Johnson et al. 2016; Nespral et al. 2016), we have recently started a RV follow-up program that aims at confirming Neptune-sized candidates detected by the K2 mission and at measuring their masses via high-precision RV follow-up observations. We here-with report the discovery of EPIC 211391664b, a transiting Neptune-sized planet in a 10-day orbit around a relatively bright ($V=12.2$ mag) solar-like star photometrically monitored by the K2 mission during its Campaign 5. We combined the K2 photometry with ground-based follow-up observations to assess the planetary nature of the transiting object and derive its mass.

The paper is organized as follows: in Sect. 2 we present the K2 photometry, whereas in Sect. 3 and 4 our ground-based photometric and spectroscopic follow-up. Sect. 5 reports on the characterization of the host star. Sect. 6 describes the joint RV and photometric analysis. Results, discussion, and conclusion are given in Sect. 7 and 8.

2. K2 LIGHT CURVE

The K2 Campaign 5 observations began on 27 April 2015 UT and lasted until 10 July 2015 UT². During the observations the boresight of the *Kepler* spacecraft was pointed at coordinates $\alpha = 08^{\text{h}}40^{\text{m}}38^{\text{s}}$, $\delta = +16^\circ 49' 47''$. A total of 26 054 light curves were simultaneously acquired by K2; 25 850 in long cadence mode (30 minute integration time) and 204 in short cadence

mode (1 minute integration time).

In this work, we used the light curves extracted by Vanderburg & Johnson (2014) from Field 5 K2 data³. We searched the light curves for transit signals using the DST algorithm (Cabrera et al. 2012) and the EXOTRANS pipeline (Grziwa et al. 2012). DST and EXOTRANS have been applied extensively to both *CoRoT* (Carpano et al. 2009; Cabrera et al. 2009; Erikson et al. 2012; Carone et al. 2012; Cavarroc et al. 2012) and *Kepler* (Cabrera et al. 2014; Grziwa & Pätzold 2016) data. All transit detection algorithms search for a pattern in the data and use statistics to assess whether a signal is present in the data or not. When compared to widely used algorithms such as, e.g., Box Least Squares (BLS; Kovács et al. 2002), DST uses an optimized transit shape, with the same number of free parameters as BLS, and an optimized statistic for signal detection. EXOTRANS uses a combination of the wavelet based filter technique VARLET (Grziwa & Pätzold 2016) and the BLS detection algorithm. VARLET was developed to reduce both stellar variability and data discontinuities.

Both DST and EXOTRANS identified a periodic transit-like signal associated with the target EPIC 211391664. The star was proposed for K2 observations by programs GO5007 (P.I.: J. Winn) and GO5029 (P.I.: D. Charbonneau). For brevity we will hereafter refer to the star and its transiting planet as C5.1664 and C5.1664b, respectively. The target passed all of the tests that we use to identify likely false positives (including lack of odd-even transit depth variations, absence of a deep secondary eclipse, and lack of large photometric variations in phase with the candidate orbital period), and so we proceeded to more detailed fitting of the light curve, as well as high-resolution imaging, reconnaissance spectroscopy, and RV observations (Sect. 3 and 4). We also searched for additional transit signals in the K2 lightcurve of this star, but none were found. The main identifiers, optical and infrared magnitudes, and proper motions of this star are listed in Table 1.

3. FASTACAM HIGH-RESOLUTION IMAGING

C5.1664 was observed on 17 May 2016 with the FAST-CAM lucky imaging camera (Oscoz et al. 2008) mounted on the 1.5m Carlos Sánchez Telescope of Teide Observatory in Tenerife (Spain). To account for the low altitude of the object at the time of our observation, we used relatively long exposure times of 300 milliseconds and acquired a total of 5 000 images. We selected the

¹ Source: exoplanet.eu.

² See <http://keplerscience.arc.nasa.gov/k2-fields.html>.

³ Publicly available at <https://www.cfa.harvard.edu/~avanderb/allk2c4obs.html>.

Table 1. Main identifiers, magnitudes, and proper motion of C5_1664.

Parameter	Value	Source
<i>Main Identifiers</i>		
EPIC	211391664	EPIC
UCAC	508-047859	EPIC
2MASS	08255719+1130402	EPIC
α (J2000.0)	08 ^h 05 ^m 57.189 ^s	EPIC
δ (J2000.0)	+11°30′40.12″	EPIC
<i>Magnitudes</i>		
<i>B</i>	12.646±0.030	EPIC
<i>V</i>	12.166±0.030	EPIC
<i>g</i>	12.313±0.030	EPIC
<i>r</i>	12.031±0.030	EPIC
<i>J</i>	11.124±0.022	2MASS
<i>H</i>	10.905±0.025	2MASS
<i>K</i>	10.869±0.028	2MASS
<i>W1</i>	10.823±0.023	WISE
<i>W2</i>	10.856±0.020	WISE
<i>W3</i>	10.678±0.108	WISE
<i>W4</i>	8.258	WISE
<i>Proper motions</i>		
$\mu_\alpha \cos \delta$ (mas yr ⁻¹)	-15.4 ± 2.3	UCAC2
μ_δ (mas yr ⁻¹)	-8.8 ± 1.5	UCAC2

NOTE—Values of fields marked with EPIC are taken from the Ecliptic Plane Input Catalog, available at <http://archive.stsci.edu/k2/epic/search.php>. Values marked with UCAC2, 2MASS, and WISE are from Zacharias et al. (2004), Cutri et al. (2003), Cutri & et al. (2013), respectively. The WISE W4 magnitude is an upper limit.

300 best images and processed them using the COELI⁴ algorithm (Cagigal et al. 2016). This algorithm reinforces the pixels whose intensity follows the same time statistics as the host star, which can only happen when the pixels contain an object.

The final image shows the target to be isolated except for the detection of an object located 1.9″ South-West of C5_1664. The nearby star is 50±10 times fainter (4.2±0.2 mag) than the main target (see Fig. 1). The 1.9″ distance between the target and the faint object is less than the sky-projected size of the *Kepler*/K2 CCD pixel (~4″). We therefore assumed that the light from the faint object contributes with a fraction of 1/(50±10) to the measured flux of C5_1664 and corrected the K2 light curve accordingly prior of performing the joint analysis presented in Sect.6.

No additional contaminants were identified. The DSS images reveal that the next closest star with a brightness comparable to the target is a ~3.5-mag fainter object

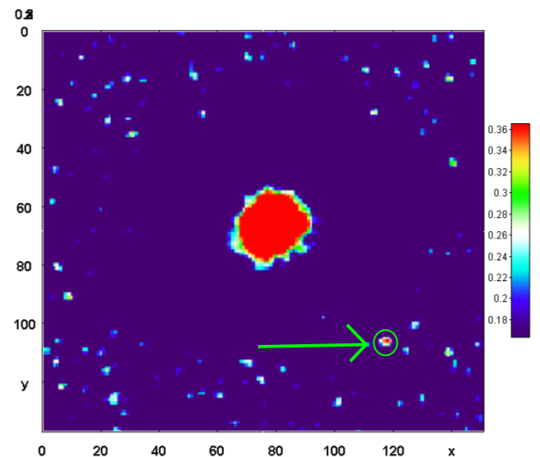


Figure 1. FASTCAM image of C5_1664 processed with COELI. The pixel scale is 0.042″; North is up, East is left. C5_1664 is in the center of the ring-shaped feature, which is an artifact of the image processing. The faint object at a distance of 1.9″ South-East is indicated with a green arrow.

that is located at ~42″ East of C5_1664, which is too large to produce any relevant influence onto the K2 light curve of C5_1664.

⁴ ImageJ Plugin: <https://imagej.nih.gov/ij/plugins/index.html>.

4. SPECTROSCOPIC FOLLOW-UP OBSERVATIONS

We took 2 reconnaissance spectra of C5_1664 with the Harlan J. Smith 2.7m Telescope and the Tull Coudé Spectrograph (Tull et al. 1995) at McDonald Observatory. The Tull spectrograph covers the entire optical spectrum (3450-9800Å) at a resolving power of $R \approx 60\,000$. We used exposure times of 1800 seconds, which resulted in a signal-to-noise ratio (SNR) of ~ 30 per pixel at 5500Å. We derived a first estimates of the spectroscopic parameters by using our code *Kea* that compares observed high-resolution spectra to a large library of synthetic models (Endl & Cochran 2016). For the first spectrum we obtained the following parameters: $T_{\text{eff}} = 5880 \pm 107$ K, $\log g_{\star} = 3.81 \pm 0.31$ (cgs), $[\text{Fe}/\text{H}] = -0.06 \pm 0.07$ dex and a $v \sin i_{\star} = 8.8 \pm 0.3$ km s $^{-1}$. For the second observation: $T_{\text{eff}} = 5820 \pm 116$ K, $[\text{Fe}/\text{H}] = -0.03 \pm 0.08$ dex, $\log g_{\star} = 4.00 \pm 0.35$ (cgs) and a $v \sin i_{\star} = 8.7 \pm 0.4$ km s $^{-1}$. We also measured an absolute RV of 76.7 ± 0.2 km s $^{-1}$ by cross-correlating the data with spectra of the RV standard star HD 50692 (Udry et al. 1999).

We also acquired 4 high-resolution spectra ($R \approx 67\,000$) in November 2015 and January 2016 using the Fibre-fed Échelle Spectrograph (FIES; Frandsen & Lindberg 1999; Telting et al. 2014) mounted at the 2.56m Nordic Optical Telescope (NOT) of Roque de los Muchachos Observatory (La Palma, Spain). We adopted the observing strategy described in Buchhave et al. (2010) and Gandolfi et al. (2015), i.e., we took 3 consecutive exposures of 1200 seconds per observation epoch – to remove cosmic ray hits – and acquired long-

exposed ($T_{\text{exp}} \approx 35$ seconds) ThAr spectra immediately before and after the three sub-exposures – to trace the RV drift of the instrument. We reduced the data using standard IRAF and IDL routines. The signal-to-noise ratio (SNR) of the extracted spectra is about ~ 30 per pixel at 5500 Å. Radial velocity measurements were derived via SNR-weighted, multi-order cross-correlation with the RV standard star HD 50692 – observed with the same instrument set-up as C5_1664. They are listed in Table 2 along with the full-width at half maximum (FWHM) and bisector span (BIS) of the cross-correlation function (CCF).

We also acquired 8 high resolution spectra using the HARPS ($R \approx 115\,000$ Mayor et al. 2003) and HARPS-N spectrographs ($R \approx 115\,000$ Cosentino et al. 2012) mounted at the ESO-3.6m telescope of La Silla observatory (Chile) and the 3.58m Telescopio Nazionale Galileo (TNG) of Roque de los Muchachos Observatory (La Palma, Spain), respectively. The observations were performed between December 2015 and May 2016, setting the exposure times to 1800–3600 seconds depending on the sky condition. We monitored the Moon background light using the second fiber and reduced the data with the dedicated HARPS and HARPS-N data reduction software pipeline. The SNR of the extracted spectra is SNR=35-45 per pixel at 5500 Å. Radial velocities (Table 2) were extracted by cross-correlation with a G2 numerical mask (Baranne et al. 1996; Pepe et al. 2002).

The FIES, HARPS, HARPS-N RVs show no significant correlation with the FWHM and BIS of the CCFs, providing evidence that the observed RV variation is caused by the Doppler reflex motion of the star.

Table 2. Radial velocity measurements

BJD _{TDB} -2450000	RV (km s $^{-1}$)	σ_{RV} (km s $^{-1}$)	CCF FWHM (km s $^{-1}$)	CCF BIS (km s $^{-1}$)	Instrument
7342.706590	76.6027	0.0082	15.1659	0.0390	FIES
7344.744082	76.6243	0.0081	15.1694	0.0401	FIES
7347.706247	76.6143	0.0082	15.1770	0.0430	FIES
7394.699773	76.6130	0.0082	15.1790	0.0366	FIES
7371.582060	76.7393	0.0077	10.3474	0.0407	HARPS-N
7371.601679	76.7324	0.0098	10.3309	0.0499	HARPS-N
7448.440479	76.7499	0.0074	10.3352	0.0456	HARPS-N
7509.495449	76.7558	0.0084	10.3567	0.0430	HARPS
7511.495428	76.7516	0.0053	10.3617	0.0442	HARPS
7512.429111	76.7313	0.0048	10.3558	0.0580	HARPS-N
7512.472984	76.7376	0.0055	10.3632	0.0450	HARPS
7516.525371	76.7425	0.0068	10.3729	0.0600	HARPS

5. PROPERTIES OF THE HOST STAR

We co-added the spectra from the NOT, ESO-3.6m, and TNG separately to get a combined FIES spectrum, a separate combined HARPS spectrum, and a third separate HARPS-N spectrum. The co-added data have a SNR of ~ 100 per pixel at 5500 Å. We used the three combined spectra to refine the estimates of the spectroscopic parameters of the host star. Following the spectral analysis of *CoRoT* and *Kepler* host stars (e.g. Fridlund et al. 2010; Gandolfi et al. 2015), we selected spectral features that are sensitive to different photospheric parameters. Our method is based on Spectroscopy Made Easy (SME), a software package that calculates synthetic spectra and fits them to high resolution observed spectra (Valenti & Piskunov 1996). SME is especially designed to determine basic stellar and atomic parameters from a match of the observed and normalized spectrum to the synthetic spectra generated from the parameterized atmospheres. It uses a non-linear least squares algorithm to solve for any subset of allowed parameters, which include atomic data ($\log gf$ and van der Waals damping constants), the model atmosphere parameters (T_{eff} , $\log g_*$), the metal abundances, and the projected rotational velocity $v \sin i_*$. The SME 4.43 distribution includes a grid with a very large set of 1D-LTE plane-parallel stellar atmospheric models (ATLAS9, ATLAS12, NextGen, and MARCS models; Kurucz 1993, 2013; Hauschildt et al. 1999; Gustafsson et al. 2008). ATLAS12 is an opacity sampling model atmosphere program that computes the same models as ATLAS9 but instead of using pre-tabulated opacities and models with arbitrary abundances, ATLAS12 uses individual abundances and line data.

Our spectral analysis begins by primarily using the wings of the H_α and H_β Balmer lines to determine T_{eff} , adopting the calibration equations of Bruntt et al. (2010) and Doyle et al. (2014) to estimate the microturbulent (V_{mic}) and macroturbulent (V_{mac}) velocities. $v \sin i_*$ is determined from a set of iron lines after which Mg I lines at $\lambda = 5167, 5173, \text{ and } 5184$ Å and Ca I lines at $\lambda = 6102, 6122, 6162, \text{ and } 6439$ Å, are used to estimate the $\log g_*$. In order to verify the accuracy of this method, we have analyzed a Solar spectrum from Wallace et al. (2011). Comparing with the discussion given in Valenti & Fischer (2005), we found the errors quoted there to be representative of what can currently be achieved when calculating synthetic spectra in order to fit high resolution, high SNR spectra.

We obtained consistent results from the FIES, HARPS, and HARPS-N well within the $1\text{-}\sigma$ uncertainty. Our final adopted values for T_{eff} , $\log g_*$, $[M/H]$, and $v \sin i_*$ are the weighted means of the values produced by the three co-added spectra and the quoted errors are

the $1\text{-}\sigma$ standard deviation. They are also consistent within $2\text{-}\sigma$ with the preliminary values derived from the 2 reconnaissance spectra taken at McDonald observatory (Sect. 4). We note that the $v \sin i_*$ estimates obtained from the McDonald spectroscopic data using KEA should be regarded as upper limits as they do not account for the line broadening induced by the macroturbulent velocity (Endl & Cochran 2016).

We determined stellar mass, radius, and age by combining the effective temperature T_{eff} and metallicity $[M/H]$ with the mean density ρ_* obtained from the transit light curve modeling (Sect. 6). We compared the position of the host star on a ρ_* -versus- T_{eff} with a fine grid of evolutionary tracks. The latter were computed *ad hoc* for this work using the FRANEC code (Tognelli et al. 2011), setting the same configuration as for the Pisa Stellar Evolution Data Base for low-mass stars⁵ (Dell’Omodarme et al. 2012). We adopted the mixing-length parameter $\alpha_{ml} = 1.74$, which is our solar calibrated value for the heavy element mixture of the Sun by Asplund et al. (2009). We accounted for microscopic diffusion by means of the routine developed by Thoul et al. (1994). The final grid contains tracks in the mass range $0.90\text{-}1.30 M_\odot$, with a step of $0.01 M_\odot$, computed for five different couples of initial metallicity Z and helium abundance Y , namely, (0.006, 0.260), (0.008, 0.265), (0.010, 0.268), (0.011, 0.271), (0.012, 0.273), and (0.013, 0.274). We found that evolutionary models with initial metal content between $Z=0.011$ and $Z=0.013$ reproduce the current photospheric metallicity. With a mass of $M_* = 1.074 \pm 0.042 M_\odot$, radius of $R_* = 1.311_{-0.048}^{+0.083} R_\odot$ and an age of $5.2_{-1.0}^{+1.2}$ Gyr (Table 3), C5-1664 is a slightly evolved F-type star leaving the main sequence. Based on the calibration of Straizys & Kuriliene (1981) for dwarf stars, the effective temperature of the star translates into a F8 V spectral type. The stellar mass and radius imply a surface gravity of $\log g_* = 4.23_{-0.05}^{+0.03}$ (cgs), which agrees within $1\text{-}\sigma$ with the value derived from the co-added spectra of $\log g_* = 4.35 \pm 0.10$ (cgs).

We checked the K2 data for evidence of rotational modulation, but could not clearly determine any period for the stellar rotation. Assuming that the star is seen equator-on, the projected rotational velocity $v \sin i_* = 6.1 \pm 0.5 \text{ km s}^{-1}$ and stellar radius $R_* = 1.311_{-0.048}^{+0.083} R_\odot$ imply a rotational period of about $P_{\text{rot}} = 10.9$ days.

Following the technique described in Gandolfi et al. (2008), we used the magnitudes listed in Table 1 and our spectroscopic parameters to estimate the interstellar extinction and distance to the star. We found

⁵ Available at <http://astro.df.unipi.it/stellar-models/>.

that the light of C5.1664 suffers a negligible reddening ($A_v=0.05\pm 0.05$ mag) and the star is located at a distance $d = 435_{-15}^{+30}$ pc from the Sun.

6. JOINT RV-TRANSIT MODELING

We performed the joint modeling of the photometric and spectroscopic data using the code `pyaneti`, a Python/Fortran software suite that finds the best fitting solution by χ^2 minimization using Markov Chain Monte Carlo (MCMC) methods (Barragán et al., in preparation). The code implements the ensemble sampler with affine invariance algorithm for a larger coverage of the parameter space (Goodman & Weare 2010).

The photometric data included in the joint analysis are subsets of the whole K2 light curve. We selected ~ 18 hours of data-points around each of the 7 transits⁶ observed by K2. We de-trended the individual transits using a second-order polynomial fitted to the out-of-transit points. The final data-set contains 180 photometric points. The modeled RV data-set contains the 12 measurements listed in Table 2.

The radial velocity model is given by a Keplerian orbit and an offset term for each systemic velocity (see, e.g., Perryman 2014). We fit for the systemic velocity γ_j (as measured by the j^{th} instrument), the RV semi-amplitude variation K , the transit epoch T_0 , the period P_{orb} , the eccentricity e , and the argument of periastron of the star’s orbit ω measured from the ascending node to its periastron.

The transit model follows the quadratic limb-darkened law of Mandel & Agol (2002). We accounted for the K2 long integration ($T_{\text{exp}}=29.425$ minutes) by super-sampling the transit model with 10 sub-sample per long cadence data (Kipping 2010). For the linear u_1 and quadratic u_2 limb darkening coefficients, we used the $q_1 = (u_1 + u_2)^2$ and $q_2 = u_1 [2(u_1 + u_2)]^{-1}$ parameterization described in Kipping (2013). The fitted transit parameters are T_0 , P_{orb} , e , ω , scaled semi-major axis a/R_\star , planet-to-star radius ratio R_p/R_\star , impact parameter b , q_1 , and q_2 .

The joint analysis was carried out by minimizing

$$\chi^2 = \sum_i^{N_{\text{RV}}} \left(\frac{\text{RV}_i - O_{\text{RV},i}}{\sigma_{\text{RV},i}} \right)^2 + \sum_i^{N_{\text{TR}}} \left(\frac{\text{TR}_i - O_{\text{TR},i}}{\sigma_{\text{TR},i}} \right)^2, \quad (1)$$

which yielded the best fitting solution for T_0 , P_{orb} , e , ω , b , a/R_\star , R_p/R_\star , q_1 , q_2 , K and γ_j .

We fitted for both a circular and eccentric model. The joint modeling was carried out running 500 independent chains with uninformative priors in the wide ranges $P_{\text{orb}} = [10.1, 10.2]$ days, $T_0 = [2457145.7, 2457146.3]$,

$b = [0, 1]$, $a/R_\star = [5, 100]$, $R_p/R_\star = [0.005, 0.2]$, $K = [0.001, 1.0]$ km s⁻¹, and $\gamma_j = [1, 100]$ km s⁻¹. For the circular model we set $e = 0$ and $\omega = 90$ deg, while for the eccentric fit we set uninformative priors between the limits $e = [0, 1]$ and $\omega = [0, 360]$ deg. For q_1 and q_2 we set uninformative priors in the range $[0, 1]$ to sample a physical solution for the limb darkening coefficients (Kipping 2013).

The chain convergence was checked by comparing the “between-chain” and “within-chain” variance using the Gelman-Rubin statistics. The burning-in phase uses 25 000 additional iterations with a thin factor of 50, leading to a final number of 500 independent points for each chain, i.e., 250 000 independent points for each fitted parameter.

An initial global fit to the data yielded the parameterized limb darkening coefficients $q_1 = 0.27_{-0.12}^{+0.29}$ and $q_2 = 0.47_{-0.24}^{+0.26}$ which corresponds to $u_1 = 0.47_{-0.17}^{+0.14}$ and $u_2 = 0.03_{-0.21}^{+0.36}$. As described in Csizmadia et al. (2013), the large uncertainties arise from the shallow transit depth ($\sim 0.1\%$), the small number of data points (~ 180) and transits (7), and the K2 long integration time (~ 30 minutes). We thus chose to constrain the limb darkening coefficient interpolating the table of Claret & Bloemen (2011) and assuming conservative 20% error bars. We stress that the system parameters derived with uninformative priors on the limb darkening coefficients are well within 1- σ from those obtained by constraining u_1 and u_2 .

7. RESULTS AND DISCUSSION

Figure 2 shows the folded transit light curves and phase-folded RV curve, along with their best fitting models. The parameter estimates and error bars are listed in Table 3. They are taken as the median of the final posterior distributions and the 68% percent of the confidence intervals (Gregory 2010).

Our RV measurements do not allow us to constrain the eccentricity of the system. A fit for an eccentric orbit yields $0.19_{-0.13}^{+0.17}$ with a significance of only $\sim 1\text{-}\sigma$. According to the **F-test** proposed by Lucy & Sweeney (1971), there is a 83% probability that the best-fitting eccentric solution could have arisen by chance if the actual orbit were circular. Moreover, we found that the circular (DOF=153) and eccentric (DOF=151) models provide very similar minimum χ^2 values of ~ 152 . The difference of the Bayesian information criterion is $\Delta\text{BIC}=10$ between the two models, implying that the circular model is favored. We therefore adopted the circular model as the one that better describes our data. We note that the derived system parameters for a non-zero eccentricity are consistent within 1- σ with those derived assuming a circular orbit.

C5.1664b has a mass of $M_p = 32.2 \pm 8.1 M_\oplus$ and a

⁶ The transit duration is ~ 5 hours.

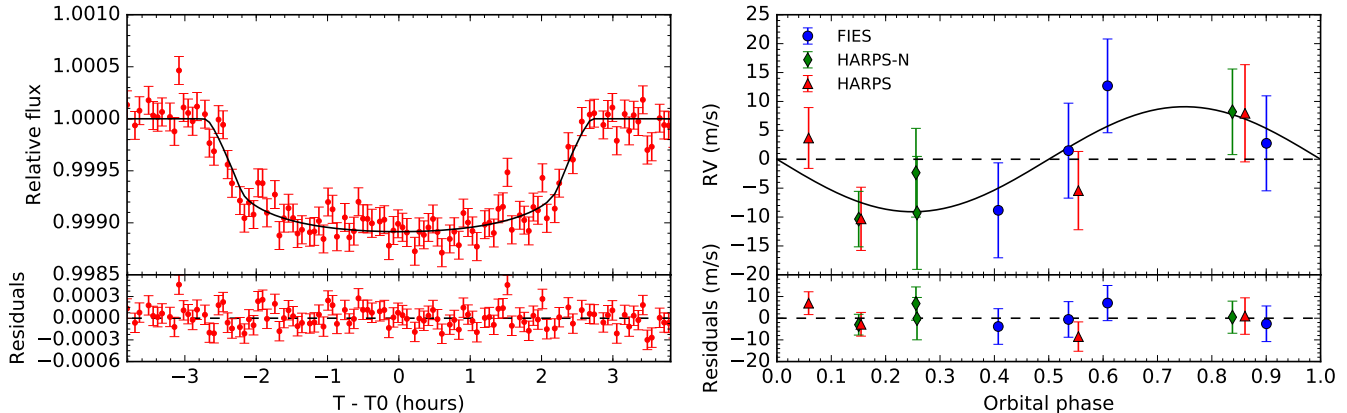


Figure 2. *Left panel:* Transit light curve folded to the orbital period of C5_1664b and residuals. The red points mark the binned K2 data and their error bars. The solid line mark the re-binned best-fitting transit model. *Right panel:* Phase-folded FIES (blue circles), HARPS-N (green diamonds) and HARPS (red triangles) RV measurements of C5_1664 and best fitting circular orbit (solid line), following the subtraction of the systemic velocities as measured from each instrument.

radius of $R_p = 4.3^{+0.3}_{-0.2} R_\oplus$, consistent with a density of $2.15^{+0.67}_{-0.60} \text{ g cm}^{-3}$. These parameters were calculated adopting the stellar mass and radius derived in Sect. 5 and listed in Table 3. Figure 3 shows the position of C5_1664b in the mass-radius diagram for Neptune-sized planets. The plot includes only those objects whose mass and radius have been estimated with a precision of at least $3\text{-}\sigma$. C5_1664b joins the family of intermediate mass ($20 < M_p < 50 M_\oplus$) Neptune-sized planets. Whereas its radius is slightly larger than that of Neptune ($3.9 R_\oplus$), the mass of C5_1664b is almost twice as large as the mass of Neptune. This implies that a solid massive core surrounded by a large atmosphere is expected (see, e.g., Weiss & Marcy 2014).

Assuming a minimum mass solar nebula (MMSN), the isolation mass (Schlichting 2014) of a planet at 0.093 AU is $\sim 0.004 M_\oplus$, which is significantly lower than the mass of C5_1664b. In order to form C5_1664b *in situ*, a disk surface density ~ 5500 times larger than the MMSN is required. This value would generate gravitational instabilities in the disk, because its Toomre factor would be $Q \approx 0.03 \ll 1$ (Schlichting 2014). This scenario does not support the *in situ* formation of C5_1664b.

Recently Valsecchi et al. (2014) proposed that Neptune-mass planets may form via migration of hot Jupiters that come so close to their host stars as to fill their Roche lobe and start conservative mass transfer to the star. This may reverse the direction of migration and increase the orbital period. However, it seems very difficult to reach a final orbital period of about 10 days, as in the case of C5_1664b. Moreover, this formation scenario cannot easily account for the measured relatively low density of the planet ($2.15^{+0.67}_{-0.60} \text{ g cm}^{-3}$). Therefore, we argue that C5_1664b likely formed in the outer region of the protoplanetary disk and then migrated inwards to its current position (see, e.g. Kley & Nelson 2012).

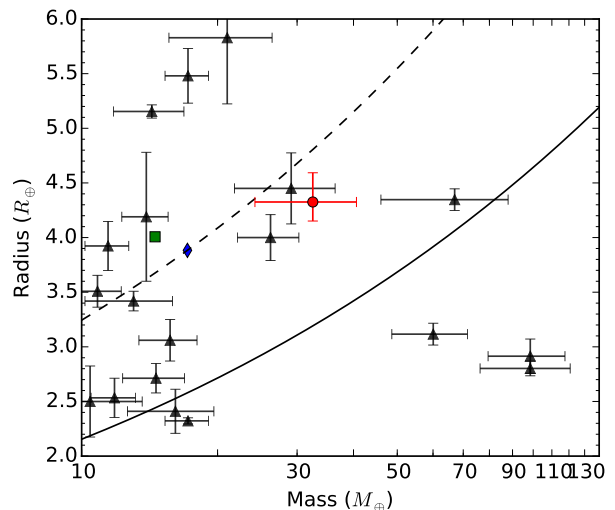


Figure 3. Mass-radius diagram for Neptune-sized planets ($2.0 \lesssim R_p \lesssim 6.0 R_\oplus$) whose mass has been determined with a $3\text{-}\sigma$ precision, as extracted from the Exoplanets Orbit Database (Han et al. 2014) (as of 25 May 2016). The red circle marks the position of C5_1664b, whereas the green diamond and blue square show the position of Neptune and Uranus, respectively. The solid and dashed lines mark the Earth (5.5 g cm^{-3}) and Neptune (1.6 g cm^{-3}) isodensity curves.

We have integrated the equations of tidal and rotational evolution as in Lanza & Mathis (2016) assuming a constant modified tidal quality factor Q'_* for the star. Given that the stellar rotation period is close to the orbital period (Sect. 5), tidal dissipation by inertial waves inside the star should be considered leading to a remarkably stronger tidal interaction than in the case of the equilibrium tide (Ogilvie & Lin 2007). Therefore, we explore the evolution for three fixed values of Q'_* , i.e., 10^5 , 10^6 , and 10^7 , from the stronger to the weaker coupling. Following Lanza et al. (2011), we included the loss of angular momentum produced by the

stellar magnetized wind considering a saturation regime for an angular velocity greater than $8\Omega_{\odot}$, where Ω_{\odot} is the present solar angular velocity. We assumed that the orbit of the planet is circular, although the tidal interaction is so weak that any initial eccentricity could survive up to the present stage of the system evolution (see below).

Fig. 4 shows the evolution of the rotation period of the star (upper panel), semi-major axis of the planet’s orbit (middle panel), and stellar radius (lower panel) as obtained from the evolutionary models presented in Sect. 5. Tidal interaction is so weak that there is virtually no evolution of the orbital separation since the planet arrived at the present semi-major axis (Fig. 4, middle panel). The rotation of the star is braked solely by the stellar wind with a completely negligible tidal exchange between the orbital and the spin angular momenta, and no dependency on the stellar tidal quality factor Q'_* , owing to the small mass of the planet and large separation. (Fig. 4, upper panel). Under our model assumptions, we estimated that the star reached the zero age main sequence (ZAMS) with a rotation period of about 1.5 days.

The tidal evolution of the planet will become important in the future – after ~ 3 Gyr from now – due to the increase of the stellar radius and rotational period of the star, leading to a rapid decay of the planet’s orbit (Fig. 4, middle panel).

The amount of angular momentum in the orbit is largely insufficient to synchronize the rotation of the star, so the present approximately synchronous state cannot be maintained. Damiani & Lanza (2015) showed that other systems having host stars with an effective temperature around 6100 K show a rather wide distribution of the ratio of the orbital period to the stellar spin period, even in the case of more massive planets, thus supporting the conclusion that the present approximate synchronicity is probably coincidental.

Finally, we considered the possibility that the planet was initially significantly closer to the star when the latter reached the ZAMS and was pushed outwards by the action of tides because angular momentum was transferred from the stellar spin to the orbit, provided that the rotational period of the star was shorter than the orbital one. We found that also this scenario is unlikely. As an illustrative case, we show in Fig. 4 two integrations for the planet initially at an orbital period of 2.5 days, corresponding to a semi-major axis of 0.037 AU. This is the minimum orbital period for observed Neptune-mass planets around main-sequence stars (cf. Fig. 4 of Valsecchi et al. 2014) that we chose in order to maximize the strength of the tidal interaction. Since the star was initially rotating faster than the planet, the tidal interaction was initially pushing the planet outwards, in

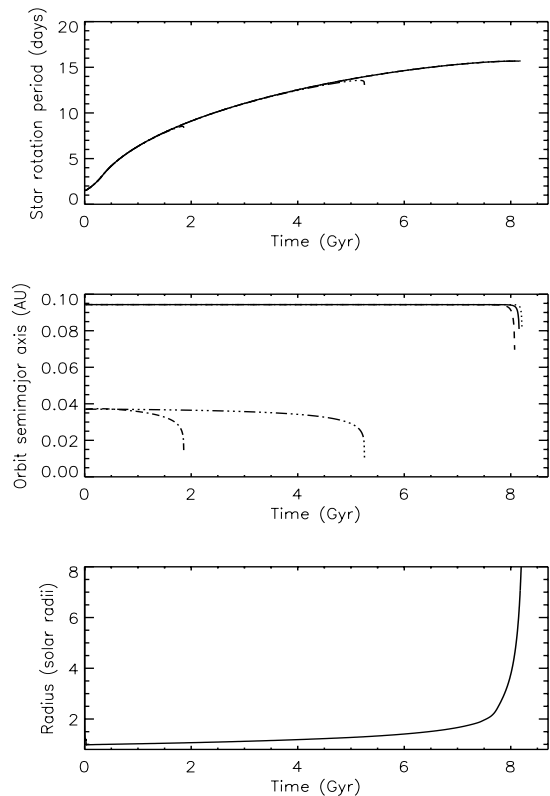


Figure 4. Rotational period of the star (upper panel), semi-major axis of the planet orbit (middle-panel), and stellar radius (lower panel) versus time. Different line styles refer to different initial semi-major axis a_0 and tidal quality factor of the star Q'_* as follows: solid line: $Q'_* = 10^6$, $a_0 = 0.0943$ AU; dotted line: $Q'_* = 10^7$, $a_0 = 0.0943$ AU; dashed line: $Q'_* = 10^5$, $a_0 = 0.0943$ AU; dash-dotted: $Q'_* = 10^5$, $a_0 = 0.037$ AU (corresponding to an orbital period of 2.5 days); dash-triple-dotted: $Q'_* = 10^6$, $a_0 = 0.037$ AU.

particular for $Q'_* = 10^5$ (Fig. 4, middle panel). However, the fast rotational braking of the star led soon to a rotation period longer than the orbital period. Since the amount of orbital angular momentum was too small to maintain the synchronous state, the final fate of the planet was to fall towards the star under the action of tides within a few Gyrs⁷. This scenario would account for the significant dearth of Neptune-like planets with orbital periods below 2-4 days (see, e.g., Szabó & Kiss 2011; Mazeh et al. 2016).

The tidal evolution of the system further supports an inward migration scenario for C5-1664b, from the outer region of the system to its current position.

⁷ We note that assuming a different initial orbital period leads to qualitatively similar scenarios. If the initial orbital period of the planet is shorter than 2.5 days (i.e., $a_0 < 0.037$ AU), tidal push is stronger, but for a shorter time interval before the rotation period of the star becomes longer than the orbital period, after which the orbit decays faster. If the planet is further out ($P_{0,\text{orb}} > 2.5$ days and $a_0 > 0.037$ AU), tides are weaker, but they can act longer before the direction of the evolution of the semi-major axis is reversed and the planet falls into the star.

8. CONCLUSIONS

We confirm the planetary nature of C5_1664b and derive the system parameters. Our results are based on photometric data from the K2 space mission combined with high-precision FIES, HARPS, and HARPS-N RV measurements and lucky imaging. C5_1664b is a transiting Neptune-sized planet in a 10-day-orbit around an F8 V leaving the main sequence. It has a mass of $M_p = 32.2 \pm 8.1 M_\oplus$ and a radius of $R_p = 4.3^{+0.3}_{-0.2} R_\oplus$, translating into a mean density of $2.15^{+0.67}_{-0.60} \text{ g cm}^{-3}$. C5_1664b joins the still relatively small number of Neptune-size planets (~ 20 objects) whose mass and radius have been determined with a precision better than $3\text{-}\sigma$.

We note that C5_1664b has been recently identified as a planet candidate by [Pope et al. \(2016\)](#) and [Barros et al. \(2016\)](#), but has not been confirmed and characterized yet. We are the first team to do so for this object. On the other hand, C5_1664b does not appear in the lists of validated objects and false positives recently published by [Crossfield et al. \(2016\)](#). This further proves how a complete list of candidates requires the use of different transit detection algorithms.

We are very grateful to Simon Albrecht for providing us with one of the HARPS-N measurement and for his valuable comments and suggestions. We are thankful to Jorge Melendez, Martin Kürster, Nuno Santos, and Xavier Bonfils who kindly agreed to exchange HARPS time with us. We express our deepest gratitude to the NOT, ESO, TNG and McDonald staff members for their unique support during the observations. Szilard Csizmadia thanks the Hungarian OTKA Grant K113117. This paper includes data taken at McDonald Observatory of the University of Texas at Austin. Based on

observations obtained *a*) with the Nordic Optical Telescope (NOT), operated on the island of La Palma jointly by Denmark, Finland, Iceland, Norway, and Sweden, in the Spanish Observatorio del Roque de los Muchachos (ORM) of the Instituto de Astrofísica de Canarias (IAC); *b*) with the Italian Telescopio Nazionale Galileo (TNG) also operated at the ORM (IAC) on the island of La Palma by the INAF - Fundación Galileo Galilei. Based on observations made with ESO Telescopes at the La Silla Observatory under programme ID 097.C-0948. The research leading to these results has received funding from the European Union Seventh Framework Programme (FP7/2013-2016) under grant agreement No. 312430 (OPTICON) and from the NASA K2 Guest Observer Cycle 1 program under grant NNX15AV58G to The University of Texas at Austin. This publication makes use of data products from the Two Micron All Sky Survey (2MASS), which is a joint project of the University of Massachusetts and the Infrared Processing and Analysis Center/California Institute of Technology, funded by the National Aeronautics and Space Administration and the National Science Foundation. This publication makes use of data products from the Wide-field Infrared Survey Explorer (WISE), which is a joint project of the University of California, Los Angeles, and the Jet Propulsion Laboratory/California Institute of Technology, funded by the National Aeronautics and Space Administration.

Facilities: Kepler (K2), NOT (FIES), ESO:3.6m (HARPS), Sanchez (FAST-CAM), Smith (TULL), TNG (HARPS-N).

Software: COELI, DST, EXOTRANS, Kea IDL, IRAF, pyaneti, SME.

REFERENCES

- Asplund M., Grevesse N., Sauval A. J., Scott P., 2009, *ARA&A*, 47, 481
- Baglin, A., Auvergne, M., Boisnard, L., et al. 2006, 36th COSPAR Scientific Assembly, 36, 3749
- Baranne, A., Queloz, D., Mayor, M., et al. 1996, *A&AS*, 119, 373
- Barros, S. C. C., Demangeon, O., & Deleuil, M. 2016, arXiv:1607.02339
- Borucki, W. J., Koch, D., Basri, G., et al. 2010, *Science*, 327, 977
- Borucki, W. J., Koch, D. G., Basri, G., et al. 2011, *ApJ*, 728, 117
- Brunnt, H., Bedding, T. R., Quirion, P.-O., et al. 2010, *MNRAS*, 405, 1907
- Buchhave, L. A., Bakos, G. A., Hartman, J. D., et al. 2010, *ApJ*, 720, 1118
- Cabrera, J., Fridlund, M., Ollivier, M., et al. 2009, *A&A*, 506, 501
- Cabrera, J., Csizmadia, S., Erikson, A., Rauer, H., & Kirste, S. 2012, *A&A*, 548, A44
- Cabrera, J., Csizmadia, S., Lehmann, H., et al. 2014, *ApJ*, 781, 18
- Cagigal, M. P., Valle, P. J., Colodro-Conde, C., Villó-Pérez, I., & Pérez-Garrido, A. 2016, *MNRAS*, 455, 2765
- Carone, L., Gandolfi, D., Cabrera, J., et al. 2012, *A&A*, 538, A112
- Carpano, S., Cabrera, J., Alonso, R., et al. 2009, *A&A*, 506, 491
- Cavarrac, C., Moutou, C., Gandolfi, D., et al. 2012, *Ap&SS*, 337, 511
- Claret A., Bloemen S., 2011, *A&A*, 529, A75
- Cochran W. D., et al., 2015, *DPS*, 47, 417.02
- Cosentino, R., Lovis, C., Pepe, F., et al. 2012, in *Society of Photo-Optical Instrumentation Engineers (SPIE) Conference Series*, Vol. 8446, Society of Photo-Optical Instrumentation Engineers (SPIE) Conference Series, 1
- Crossfield, I. J. M., Ciardi, D. R., Petigura, E. A., et al. 2016, arXiv:1607.05263
- Csizmadia, S., Pasternacki, T., Dreyer, C., et al. 2013, *A&A*, 549, A9
- Cutri, R. M., Skrutskie, M. F., van Dyk, S., et al. 2003, in “2MASS All-Sky Catalog of Point Sources”, NASA/IPAC Infrared Science Archive

Table 3. Stellar and Planetary Parameters

Parameter	Value
<i>Model Parameters</i>	
Orbital period P_{orb} (days)	10.13675 ± 0.00033
Transit epoch T_0 (BJD _{TDB} - 2 450 000)	7145.9807 ± 0.0012
Scaled semi-major axis a/R_*	$15.388^{+0.543}_{-1.192}$
Scaled planet radius R_p/R_*	$0.0301^{+0.0004}_{-0.0003}$
Impact parameter, b	$0.27^{+0.17}_{-0.14}$
Parameterized limb-darkening coefficient q_1^a	0.40 ± 0.05
Parameterized limb-darkening coefficient q_2^a	0.26 ± 0.05
Eccentricity e	0 (fixed)
Radial velocity semi-amplitude variation K (m s ⁻¹)	9.1 ± 2.3
Systemic velocity γ_{FIES} (km s ⁻¹)	76.6116 ± 0.0029
Systemic velocity γ_{HARPS} (km s ⁻¹)	76.7479 ± 0.0022
Systemic velocity $\gamma_{\text{HARPS-N}}$ (km s ⁻¹)	76.7417 ± 0.0026
<i>Derived parameters</i>	
Semi-major axis of the planetary orbit a (AU)	$0.0943^{+0.0061}_{-0.0052}$
Transit duration τ_{14} (hours)	$5.03^{+0.05}_{-0.04}$
Transit ingress/egress duration $\tau_{12} = \tau_{34}$ (hours)	$0.16^{+0.03}_{-0.01}$
Orbit inclination along the line-of-sight i_p (°)	$89.0^{+0.5}_{-0.7}$
<i>Stellar parameters</i>	
Star mass M_* (M_\odot)	1.074 ± 0.042
Star radius R_* (R_\odot)	$1.311^{+0.083}_{-0.048}$
Surface gravity $\log g_*$ (cgs) ^b	$4.23^{+0.03}_{-0.05}$
Mean density ρ_* (g cm ⁻³)	$0.66^{+0.07}_{-0.12}$
Star age (Gyr)	$5.2^{+1.2}_{-1.0}$
Spectral type ^c	F8 V
Effective temperature T_{eff} (K)	6120 ± 80
Iron abundance [Fe/H] (dex)	-0.2 ± 0.1
Nickel abundance [Ni/H] (dex)	-0.1 ± 0.1
Silicon abundance [Si/H] (dex)	-0.1 ± 0.1
Calcium abundance [Ca/H] (dex)	-0.1 ± 0.1
Sodium abundance [Na/H] (dex)	-0.0 ± 0.1
Magnesium abundance [Mg/H] (dex)	-0.0 ± 0.1
Microturbulent velocity v_{mic} ^c	1.3 ± 0.1
Macroturbulent velocity v_{mac} ^d	3.7 ± 0.6
Projected rotational velocity $v \sin i_*$	6.1 ± 0.5
Distance d (pc)	435^{+30}_{-15}
Visual interstellar extinction A_v (mag)	0.05 ± 0.05
<i>Planetary parameters</i>	
Planet mass M_p (M_\oplus)	32.2 ± 8.1
Planet radius R_p (R_\oplus)	$4.3^{+0.3}_{-0.2}$
Planet density ρ_p (g cm ⁻³)	$2.15^{+0.67}_{-0.60}$
Equilibrium temperature T_{eq} (K)	1102^{+26}_{-20}

NOTE—The adopted Sun and Earth units follow the recommendations from the International Astronomical Union (Prsa et al. 2016).

^aThe limb-darkening coefficient parameterization follows Kipping (2013). The estimates have been obtained assuming $u_1 = 0.33 \pm 0.06$ and $u_2 = 0.30 \pm 0.06$ for the linear and quadratic limb-darkening coefficients (Claret & Bloemen 2011), adopting 20 % conservative error bars.

^bStellar surface gravity $\log g_*$ as measured from the global fit and evolutionary tracks. The spectroscopic analysis gives $\log g_* = 4.35 \pm 0.10$ (cgs).

^cBased on the spectral type vs. effective temperature calibration of Straizys & Kuriliene (1981) for dwarf stars.

^dMicro and macroturbulent velocities from the calibration equations of Bruntt et al. (2010) and Doyle et al. (2014), respectively.

- Cutri R. M., et al., 2013, *yCat*, 2328
- Damiani, C., & Lanza, A. F. 2015, *A&A*, 574, A39
- Dell’Omodarme, M., Valle, G., Degl’Innocenti, S., Prada Moroni, P. G. 2012, *A&A*, 540, A26
- Doyle, A. P., Davies, G. R., Smalley, B., Chaplin, W. J., & Elsworth, Y. 2014, *MNRAS*, 444, 3592
- Endl, M., & Cochran, W. D. 2016, *PASP*, 128, 094502
- Erikson, A., Santerne, A., Renner, S., et al. 2012, *A&A*, 539, A14
- Ford E. B., et al., 2011, *ApJS*, 197, 2
- Frandsen, S. & Lindberg, B. 1999, in “Astrophysics with the NOT”, proceedings Eds: Karttunen, H. & Piirola, V., anot. conf, 71
- Fridlund, M., Hébrard, G., Alonso, R., et al. 2010, *A&A*, 512, A14
- Gandolfi D., et al., 2008, *ApJ*, 687, 1303-1322
- Gandolfi, D., Parviainen, H., Deeg, H. J. et al., 2015, *A&A*, 576, A11
- Goodman, J. & Weare, J. 2010, *Comm. App. Math. Comp. Sci.*, 5, 65
- Gregory, P. 2010, *Bayesian Logical Data Analysis for the Physical Sciences*, by Phil Gregory, Cambridge, UK: Cambridge University Press, 2010,
- Grziwa, S., Pätzold, M., & Carone, L. 2012, *MNRAS*, 420, 1045
- Grziwa, S., Gandolfi, D., Csizmadia, S., et al. 2015, *arXiv:1510.09149*
- Grziwa, S., & Pätzold M. 2016, *arXiv:1607.08417*
- Gustafsson, B., Edvardsson, B., Eriksson, K., et al. 2008, *A&A*, 486, 951
- Han, E., Wang, S. X., Wright, J. T., et al. 2014, *PASP*, 126, 827
- Hatzes, A. P. 2016, *SSRv*,
- Hauschildt, P. H., Allard, F., & Baron, E. 1999, *ApJ*, 512, 377
- Howell, S. B., Sobeck, C., Haas, M., et al. 2014, *PASP*, 126, 398
- Johnson M. C., et al., 2016, *AJ*, 151, 171
- Kipping, D. M. 2010, *MNRAS*, 408, 1758
- Kipping, D. M. 2013, *MNRAS*, 435, 2152
- Kley, W., & Nelson, R. P. 2012, *ARA&A*, 50, 211
- Kovács, G., Zucker, S., & Mazeh, T. 2002, *A&A*, 391, 369
- Kurucz, R. 1993, *ATLAS9 Stellar Atmosphere Programs and 2 km/s grid*. Kurucz CD-ROM No. 13. Cambridge, Mass.: Smithsonian Astrophysical Observatory, 1993., 13,
- Kurucz, R. L. 2013, *Astrophysics Source Code Library*, *ascl:1303.024*
- Lanza, A. F., Damiani, C., & Gandolfi, D. 2011, *A&A*, 529, A50
- Lanza, A. F., & Mathis, S. 2016, *arXiv:1606.08623*
- Lucy L. B., Sweeney M. A., 1971, *AJ*, 76, 544
- Mandel, K., & Agol, E. 2002, *ApJL*, 580, L171
- Marcy, G. W., Weiss, L. M., Petigura, E. A., et al. 2014, *Proceedings of the National Academy of Science*, 111, 12655
- Mayor, M., Pepe, F., Queloz, D., et al. 2003, *The Messenger*, 114, 20
- Mazeh, T., Holczer, T., & Faigler, S. 2016, *A&A*, 589, A75
- Mayor M., Queloz D., 1995, *Natur*, 378, 355
- Nespral D., et al., 2016, *arXiv*, *arXiv:1604.01265*
- Ogilvie, G. I., & Lin, D. N. C. 2007, *ApJ*, 661, 1180
- Osoz, A., Rebolo, R., López, R., et al. 2008, *Proc. SPIE*, 7014, 701447
- Pepe, F., Mayor, M., Galland, F. et al. 2002, *A&A*, 388, 632
- Perryman, M. 2014, *The Exoplanet Handbook*, by Michael Perryman, Cambridge, UK: Cambridge University Press, 2014
- Pope, B. J. S., Parviainen, H., & Aigrain, S. 2016, *MNRAS*,
- Prsa, A., Harmanec, P., Torres, G., et al. 2016, *arXiv:1605.09788*
- Sanchis-Ojeda R., et al., 2015, *ApJ*, 812, 112
- Schlichting, H. E. 2014, *ApJL*, 795, L15
- Straizys, V. & Kuriliene, G. 1981, *Ap&SS*, 80, 353
- Szabó G. M., Kiss L. L., 2011, *ApJ*, 727, L44
- Telting, J. H., Avila, G., Buchhave, L., et al. 2014, *AN*, 335, 41
- Thoul, A. A., Bahcall, J. N. & Loeb, A. 1994, *ApJ*, 421, 828
- Tognelli, E., Prada Moroni, P. G. & Degl’Innocenti, S. 2011, *A&A*, 533, A109
- Torres, G., Andersen, J., & Giménez, A. 2010, *A&A Rv*, 18, 67
- Tull, R. G., MacQueen, P. J., Sneden, C., & Lambert, D. L. 1995, *PASP*, 107, 251
- Udry S., Mayor M., Queloz D., 1999, *ASPC*, 185, 367
- Valenti, J. A., & Piskunov, N. 1996, *A&AS*, 118, 595
- Valenti, J. A., & Fischer, D. A. 2005, *ApJS*, 159, 141
- Valsecchi, F., Rasio, F. A., & Steffen, J. H. 2014, *ApJL*, 793, L3
- Vanderburg, A., & Johnson, J. A. 2014, *PASP*, 126, 948
- Wallace, L., Hinkle, K. H., Livingston, W. C., & Davis, S. P. 2011, *ApJS*, 195, 6
- Weiss, L. M., & Marcy, G. W. 2014, *ApJL*, 783, L6
- Winn, J. N., & Fabrycky, D. C. 2015, *ARA&A*, 53, 409
- Zacharias, N., Urban, S. E., Zacharias, M. I., et al. 2004, *AJ*, 127, 3043